CHEMISTRY OF MATERIALS

Intercalation Chemistry of the Disordered Rocksalt $Li_3V_2O_5$ Anode from Cluster Expansions and Machine Learning Interatomic Potentials

Xingyu Guo, Chi Chen, and Shyue Ping Ong*

Cite This: https://doi.org/10.1021/acs.chemmater.2c02839 Read Online

ABSTRACT: Disordered rocksalt (DRX) $Li_3V_2O_5$ is a promising anode candidate for rechargeable lithium-ion batteries because of its low voltage, high rate capability, and good cycling stability. Herein, we present a comprehensive study of the intercalation chemistry of the DRX-$Li_3V_2O_5$ anode using density functional theory (DFT) calculations combined with machine learning cluster expansions and interatomic potentials. The predicted voltage profile of the DRX $Li_3V_2O_5$ anode at room temperature based on Monte Carlo simulations with a fitted cluster expansion model is in good agreement with experiments. In contrast to previous DFT results, we find that Li ions predominately intercalate into tetrahedral sites during charging, while a majority of Li and V ions at octahedral sites remain stable. In addition, molecular dynamics simulations with a fitted moment tensor potential attribute the fast-charging capability of DRX-$Li_3V_2O_5$ to the facile diffusivity of Li^+ via a tetrahedral−octahedral−tetrahedral pathway. We further suggest tuning the Li:V ratio as a means of trading off increased lithiation capacity and decreased anode voltage in this system. This work provides in-depth insights into the high-performance DRX-$Li_3V_2O_5$ anode and paves the way for the discovery of other disordered anode materials.

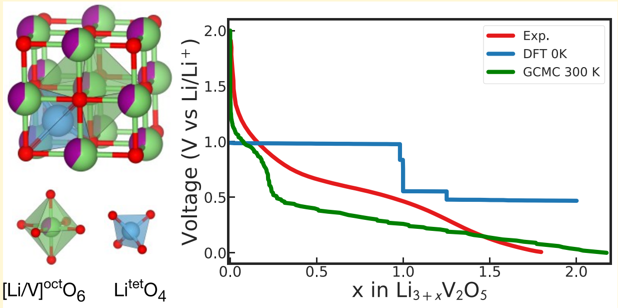

■ INTRODUCTION

Rocksalt oxides have been extensively studied as electrodes for rechargeable lithium-ion batteries (LIBs).[1] As the name implies, the O^{2-} anions in rocksalt oxides are arranged in a close-packed face-centered-cubic (fcc) framework, with the cations occupying the tetrahedral and octahedral interstitial sites, as shown in Figure 1a. For instance, the common layered transition metal (M) oxide $LiMO_2$ cathode used in LIBs is formed by an ordered arrangement of Li and M in this framework. In the past decade or so, lithium-rich disordered rocksalt (DRX) oxides have emerged as a promising class of electrode materials with high specific capacities and high rate capabilities.[1−4]

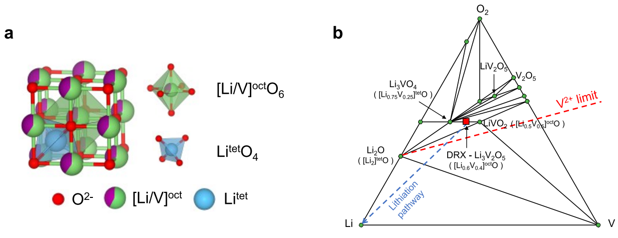

Figure 1. (a) Crystal structure of disordered rocksalt $Li_{3+x}V_2O_5$: red for O^{2-} anions forming an fcc sublattice, light blue for Li^+ in tetrahedral interstitials, and green/purple for disordered Li^+/V^{2+-4+} in octahedral interstitials. (b) Calculated phase diagram of the Li−V−O chemical system at 0 K. The green circles refer to ground states, and the red square refers to the metastable phase. The red dashed line refers to the limit of the V^{2+} oxidation state. The blue dashed line refers to the lithiation pathway in DRX-$Li_3V_2O_5$.

While DRX materials have been extensively studied as cathodes, relatively few have been explored as anodes.[5−7] Among the most promising is DRX-$Li_3V_2O_5$, recently reported by Liu et al.[5] The DRX-$Li_3V_2O_5$ anode operates at a near-optimal average voltage of ∼0.6 V versus Li/Li^+, high enough to alleviate the safety concerns attributed to Li plating that occurs during fast charging and discharging of the commercial graphite anode used in LIBs. At the same time, it is substantially lower than the 1.5 V operating voltage of lithium titanate, thereby yielding a much higher energy density.

Despite its great promise, ambiguity about the intercalation chemistry of DRX-$Li_3V_2O_5$ remains. Previously, Zheng et al.[8]

Received: September 15, 2022
Revised: February 2, 2023

proposed that the related DRX-$Li_{0.78+x}V_{0.75}O_2$ anode undergoes a conversion-type reaction, in which the single-phase material is converted into VO_2 and Li_2O as it is charged to 0.55 V versus Li/Li^+. However, our previous density functional theory (DFT) calculations attributed the low voltage and high rate capability of DRX-$Li_3V_2O_5$ to a redistributive lithium intercalation mechanism with low energy barriers.[5] These initial conclusions were reached on the basis of 0 K DFT calculations with small model cells, which did not fully explore the configurational space of the DRX anode at finite temperatures.

In this work, we revisit the intercalation chemistry of DRX-$Li_{3+x}V_2O_5$ ($0 \leq x \leq 2$) at finite temperatures using large-scale simulations with machine learning (ML) energy models. Monte Carlo simulations using a fitted cluster expansion model predict that Li primarily inserts into the tetrahedral sites of DRX-$Li_3V_2O_5$ while Li occupancy in octahedral sites remains largely unchanged, in contrast with earlier DFT results. Molecular dynamics (MD) simulations using a ML interatomic potential reveal that Li^+ diffusivity reaches its maximum at intermediate states of charge but sharply decreases at the start of charging and discharging. The high rate capability and superior cycling stability of DRX-$Li_3V_2O_5$ anode are a result of facile diffusion of Li ions through a tetrahedral−octahedral−tetrahedral pathway, consistent with previous nudged elastic band calculations.

■ METHODS

Structure Model. Figure 1a shows the crystal structure of DRX-$Li_{3+x}V_2O_5$, which has an fcc lattice in space group $Fm\bar{3}m$. The O^{2-} anions occupy the 4*a* sites. The initial composition of $Li_3V_2O_5$ has a cation:anion ratio of 1:1. On the basis of our previous studies, the lowest-DFT energy structure is one in which all Li/V cations fully occupy the octahedral 4*b* sites.[5] Henceforth, we will use the anion-normalized composition, e.g., $[Li_{0.6}V_{0.4}]^{oct}O$ for $Li_3V_2O_5$, to emphasize the site occupancies. During charging, inserted Li^+ ions also occupy the tetrahedral 8*c* sites, forming $Li^{tet}{}_x[Li_yV_{0.4}]^{oct}O$.

For more costly DFT and climbing image nudged elastic band (NEB) calculations, a set of 64 special quasi-random structures (SQSs)[9] with a formula of $Li_{19}V_{13}O_{32}$ (corresponding to $[Li_{0.59375}V_{0.40625}]^{oct}O$) were generated using 2 × 2 × 2 supercells of the conventional rocksalt cubic unit cell. The three relaxed SQS structures with the lowest energies were used for site energy and migration barrier calculations.

Density Functional Theory Calculations. Spin-polarized DFT calculations were performed using the Vienna *ab initio* simulation (VASP) package within the projector-augmented wave method.[10,11] The Perdew−Burke−Ernzerhof (PBE) functional[12] was used for the structural relaxation and electronic energy calculations with an effective Hubbard U[13,14] value of 3.25 eV for V, which is in line with the parameters used in the Materials Project.[15] All calculations were initialized in a ferromagnetic high-spin configuration. A plane wave energy cutoff of 450 eV and a *k*-point density of at least 100 per reciprocal volume were adopted. The electronic energies and forces were converged to 10^{-5} eV and 0.02 eV $Å^{-1}$, respectively.

Li Site Energies. The Li site energies were determined by inserting one Li^+ into each symmetrically distinct tetrahedral site of the three lowest-energy SQSs. The Li^{tet} site energies are given by the following expression:

$$E_{Li^{tet}} = E_{Doped} - E_{Host} - E^0_{Li} \tag{1}$$

where E_{Doped}, E_{Host}, and E^0_{Li} are the DFT-calculated energies of the SQS with one Li atom inserted into the tetrahedral site, the SQS, and the Li metal, respectively.

Order Parameter. To quantify the degree of ordering, the average Steinhardt order parameter ($\bar{D}_j$)[16] over all atoms in each structure was calculated. The Steinhardt order parameter D_j for each atom j and the bounded atom k in the structure is given by

$$D_j = \frac{1}{n^j_b} \sum_{k \in \text{bonded}} (S_{ij} + S_{kk} - 2S_{jk}) \tag{2}$$

$$S_{jk} = \sum_{-l \leq m \leq l} q^j_{lm} (q^k_{lm})^* \tag{3}$$

where S_{jk} is the correlation between atoms j and k and n^j_b is the number of atoms bonded to atom j. For the fcc cation lattice, $n^j_b = 12$ and $l = 6$. For a perfect ordered crystal such as the layered $R\bar{3}m$ $LiVO_2$, $\bar{D}_j = 0$. The higher the degree of disordering of a system, the larger the value of $\bar{D}_j$. For example, in a glass material, $\bar{D}_j$ ranges from 0.2 to 0.3.[16] In this work, $\bar{D}_j$ was calculated using the pyscal package.[17]

Cluster Expansion. A cluster expansion (CE) lattice model[18−21] for the DRX-$Li^{tet}{}_x[Li_yV_{0.4}]^{oct}O$ system was parametrized using the Clusters Approach to Statistical Mechanics (CASM) software.[22,23] The DFT-calculated total energies of the structural configurations were mapped into an expansion of crystal basis functions $\Phi(\vec{m}, \vec{\sigma})$ as given by

$$E(\vec{\sigma}) = \sum_{\vec{m}} V(\vec{m}) \Phi_\alpha(\vec{m}, \vec{\sigma}) \tag{4}$$

where $\Phi(\vec{m}, \vec{\sigma}) = \prod_{n=1}^{N} \phi(n, m_n, \sigma_n)$ is a polynomial of site basis functions $\phi(n, m_n, \sigma_n)$ and $V(\vec{m})$ are the fitted effective cluster interactions (ECIs).

To fit the CE, the $[Li/V/Va]^{oct}$ and $[Li/Va]^{tet}$ (Va: vacancy) configurations of different compositions were exhaustively enumerated in cubic rocksalt supercells up to a maximum cell size of 25 times the primitive unit cell size. It should be noted that V is allowed to occupy only the 4*b* octahedral sites, given that its occupancy at tetrahedral sites is extremely energetically unfavorable ($E_{V^{tet}} \sim 3$ eV). Li can occupy either the 4*b* octahedral or 8*c* tetrahedral sites. We note that only structures with a basis deformation of <0.1 were used in the fit, which is a typical threshold used to identify structures that match with the primitive unit cell. The basis deformation is determined by the mean-square atomic displacement relative to the positions of the ideal ions in a cubic rocksalt lattice.[22] A set of 1500 DFT-calculated energies of Li_xV_yO were used to fit an initial CE model. The model was then improved iteratively by adding more data obtained from Monte Carlo (MC) simulations. Structures that were predicted by the CE model to exhibit energies below the convex hull of >20 meV $atom^{-1}$ were then added to the training data set, and further DFT calculations were carried out on the new structures. An updated CE model was then refitted. This procedure is repeated until no new ground state structures were predicted by the CE model. As shown in Figure 3b, the fitted cluster expansion model and DFT predict the same ground state structures. In total, DFT-computed energies of ∼4500 symmetrically distinct configurations were used to fit the ECIs. All symmetrically distinct pairs, triplets, and quadruplets in the rocksalt cell within radii of 7.1, 4.1, and 4.1 Å, respectively, were used to construct the CE model.

The ECIs were obtained from an L_1 regularized linear regression fit with $\alpha = 10^{-8}$ to minimize overfitting (Figure S4). The cross-validation mean absolute error in energies is 8.94 meV $atom^{-1}$.

The calculated formation energy of $Li_{3+x}V_2O_5$ structures is given by

$$E_{form}[Li_{3+x}V_2O_5] = E[Li_{3+x}V_2O_5] - \left(1 - \frac{x}{2}\right) E[Li_3V_2O_5] - \frac{x}{2} E[Li_5V_2O_5] \tag{5}$$

Monte Carlo Simulations. MC simulations were performed using the fitted cluster expansion model. A 5 × 5 × 5 supercell (2000 sites) was used for these simulations; larger supercells produced similar results (see Figure S5). Canonical MC simulations were performed at the $[Li_{0.6}V_{0.4}]^{oct}O$ composition to probe the temperature under which the system undergoes an order−disorder transition.

Semigrand canonical MC (GCMC) simulations at 300 K were performed to study the intercalation of Li ions into the DRX-$Li_3V_2O_5$

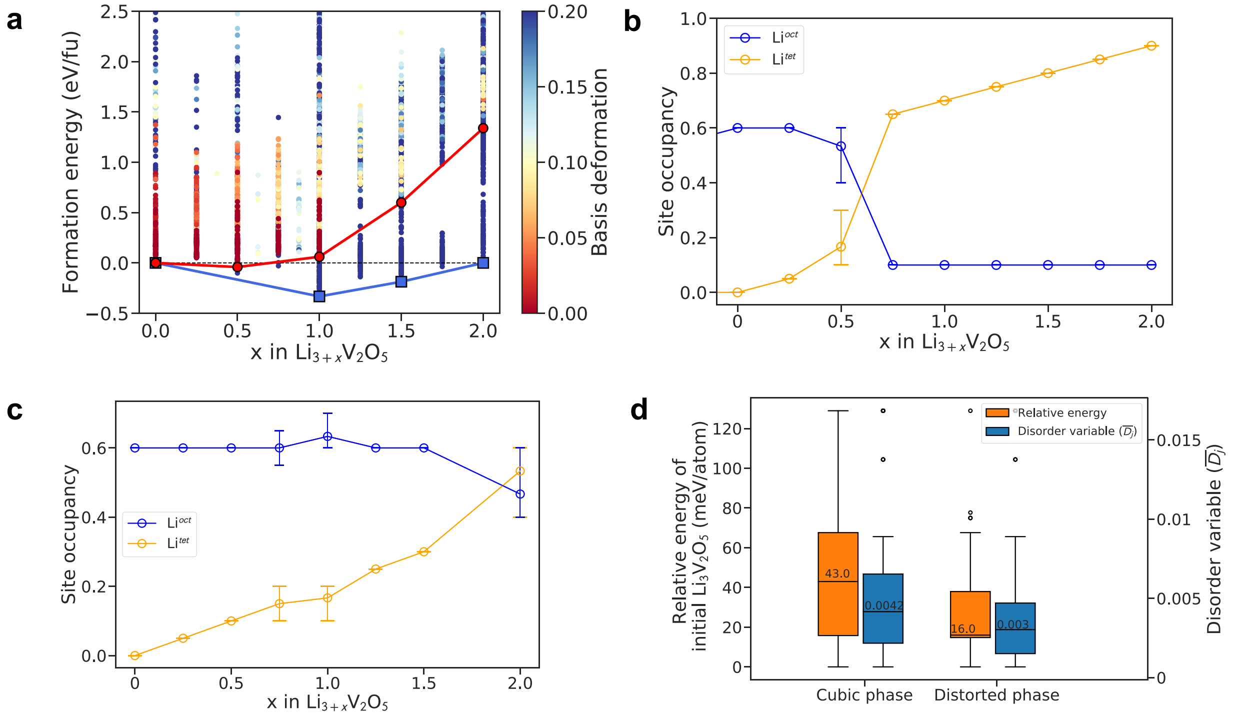

Figure 2. (a) DFT-calculated pseudobinary $Li_3V_2O_5$−$Li_5V_2O_5$ compound phase diagram. The configurations are colored in terms of their basis deformation. The red line represents the convex hull of the cubic phase, i.e., structures with low basis deformations (<0.1). The blue line represents the convex hull of all of the DFT-relaxed structures. (b) Evolution of the occupancy of Li^{oct} and Li^{tet} within $Li_3V_2O_5$−$Li_5V_2O_5$ at 0 K. (c) Evolution of the occupancy of Li^{oct} and Li^{tet} within $Li_3V_2O_5$−$Li_5V_2O_5$ in the cubic phase. At each composition, the three lowest-energy structures were used for site occupancy calculations. The average values with error bars are shown in the plot. The most stable structures of ground states and the metastable cubic phase of $Li_{3+x}V_2O_5$ (x = 0, 1, or 2) are shown in Figure S3. (d) Distribution of DFT relative energies and average Steinhardt order parameter $\overline{D}_j$ of the initial $Li_3V_2O_5$ structures corresponding to the cubic and distorted lithiated $Li_{3+x}V_2O_5$ ($x \geq 1$) structures. For each composition, no more than 50 structures with the lowest energies were used for the analysis.

structure. In a semigrand canonical ensemble, the composition and energy of the system with a fixed number of sites were allowed to fluctuate while the temperature (T) and the chemical potentials of Li (μ_{Li}) and V (μ_V) were externally imposed. The chemical potentials were referenced to that of bulk Li and V metals, for which $\mu_{Li} = \mu_V = 0$. The semi-GCMC simulations were carried out by scanning μ_{Li} with a step of $\delta\mu_{Li} = 0.01$ eV at a constant μ_V within the following chemical potential ranges: $-2.0 \leq \mu_{Li} \leq 0.0$ and $-2.0 \leq \mu_V \leq 0.0$ at 300 K. The initial disordered structures were obtained from equilibrated semi-GCMC simulations by heating the system from 5 to 1500 K at fixed chemical potentials. In this work, the semi-GCMC simulations were performed on only Li and vacancy occupancy in the tetrahedral and octahedral sites, while all V ions were fixed in the initial equilibrated octahedral sites due to the large V migration barriers.

The voltage of an electrochemical cell was related to the Li chemical potential of the electrodes according to the Nernst equation:

$$V = -(\mu_{Li} - \mu_{Li}^0)/e \tag{6}$$

where μ_{Li} is the chemical potential of Li in DRX-$Li_{3+x}V_2O_5$, μ_{Li}^0 is the reference chemical potential of Li metal, and e is the elementary charge.

Moment Tensor Potential. A machine learning interatomic potential (ML-IAP) based on the moment tensor potential (MTP) formalism[24] was developed for DRX-$Li_{3+x}V_2O_5$ using a protocol similar to that developed by Qi et al.[25] for lithium superionic conductors. The initial training structures included DFT-calculated ground state structures in the Li−V−O chemical space (supercells of Li_2O, Li_3VO_4, LiV_2O_5, and $LiVO_2$ with lattice parameters of >10 Å). To further sample the energy landscape of different Li/V arrangements, a set of SQSs with compositions of $Li_{19}V_{13}O_{32}$ ($[Li_{0.59375}V_{0.40625}]^{oct}O \approx Li_3V_2O_5$), $Li_{25}V_{13}O_{32}$ ($[Li_{0.1875}]^{tet}[Li_{0.59375}V_{0.40625}]^{oct}O \approx Li_4V_2O_5$), and $Li_{32}V_{13}O_{32}$ ($[Li_{0.40625}]^{tet}[Li_{0.59375}V_{0.40625}]^{oct}O \approx Li_5V_2O_5$) were generated in 2 × 2 × 2 supercells of the conventional rocksalt cubic unit cell. It should be noted that changes in the occupancy of tetrahedral and octahedral sites in SQSs can occur upon DFT relaxation. The SQS with the lowest-energy configuration of each composition was included in the fitting procedure.

Non-spin-polarized *ab initio* molecular dynamics (AIMD) simulations using *NVT* ensembles were performed on relaxed supercells of all initial structures with a plane wave energy cutoff of 280 eV and a gamma *k*-point. To diversify the sampled local environments, the simulations were carried out at three strains (0 ± 0.05) and four temperatures (300−1200 K at intervals of 300 K). All simulations were performed for at least 30 ps with a 2 fs time step using a Nose-Hoover thermostat.[26,27] The training structures were collected from 15 ps equilibrated runs at 0.1 ps intervals, and more accurate energies and forces were obtained by static self-consistent calculations with a *k*-point density of at least 100 per reciprocal volume and an energy cutoff of 520 eV.

Molecular Dynamics Simulations. MD simulations were performed in the *NPT* ensemble to investigate Li^+ diffusion in DRX-$Li_3V_2O_5$ using the fitted MTP potential. The time step of all MD calculations was set to 1 fs, and the total simulation time was at least 1 ns. The diffusivity (D_{Li^+}) of Li^+ was calculated by performing a linear fitting of the mean square displacement (MSD) versus $2dt$:

$$D = \frac{1}{2dt}\left\langle [\Delta r(t)]^2 \right\rangle \tag{7}$$

where d is the dimensionality factor, which equals 3 for bulk structures. $\langle[\Delta r(t)]^2\rangle$ is the average MSD over time t. Activation energy E_a was determined by the Arrhenius relationship

$$D = D_0 \exp(-E_a/kT) \tag{8}$$

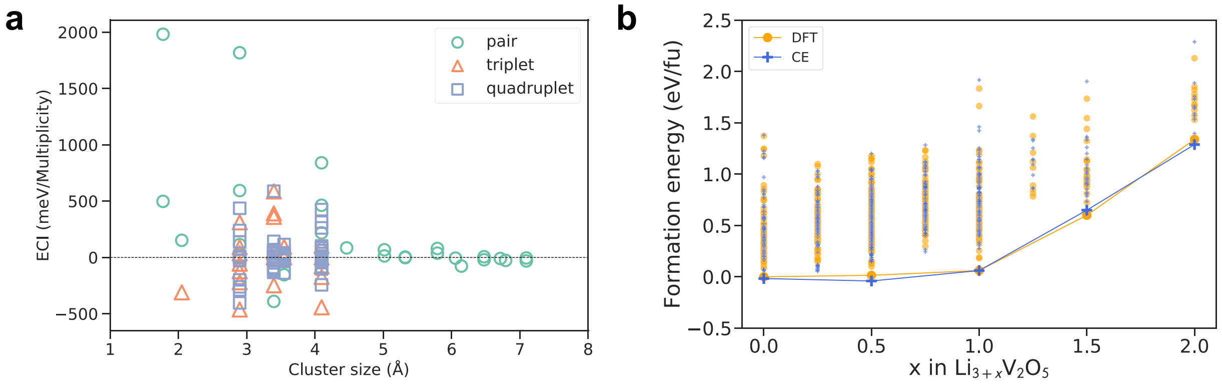

Figure 3. (a) Fitted effective cluster interaction (ECI) values with respect to the size of the clusters. (b) DFT-calculated and cluster expansion (CE)-predicted formation energies of $Li_{3+x}V_2O_5$ (x = 0.0−2.0).

where D_0 is the maximum diffusivity at infinite temperature, k is the Boltzmann constant, and T is the temperature.

All of the training, evaluations, and MD simulations were performed using MLIP,[28,29] Large-scale Atomic/Molecular Massively Parallel Simulator (LAMMPS),[30] and the open-source Materials Machine Learning (maml) Python package.[31]

Diffusion Barriers. The migration barriers of Li^+ and V^{n+} (n = 3 or 4) vacancies were calculated using the climbing image nudged elastic band (CI-NEB) method.[32,33] All NEB calculations were performed in three SQSs with the lowest DFT total energy created in the previous sections. For Li^+ migration barriers, the starting point of each NEB calculation was determined by inserting one Li^+ into the tetrahedral site, and then the structure was fully relaxed. Five linearly interpolated intermediate images were used to generate the initial guess for the minimum energy path. For Li_{tet} in varied local environments, the energy barriers for Li^+ hopping were calculated in three configurations with the lowest Li_{tet} site energy. The kinetically resolved activation (KRA)[34] Li^+ migration barrier (ΔE_{KRA}), which is independent of hop direction, was determined by the following expression:

$$\Delta E_{KRA} = E(\sigma_t) - \frac{1}{2}[E(\sigma_i + E(\sigma_f)] \tag{9}$$

where $E(\sigma_t)$, $E(\sigma_i)$, and $E(\sigma_f)$ refer to the energy of the activated transition state, the initial state, and the end state, respectively, from the CI-NEB calculations. The PBE functional without Hubbard U was adopted to avoid the possible mixing of the diffusion barrier with a charge transfer barrier.[35] The force and energy convergence criteria were 0.05 eV/Å and 5×10^{-5} eV, respectively.

■ RESULTS

Li−V−O Phase Diagram. Figure 1b shows the DFT-calculated Li−V−O phase diagram at 0 K. $Li_3V_2O_5$ ($[Li_{0.6}V_{0.4}]^{oct}O$), represented by the red square, is unstable at 0 K relative to $LiVO_2$ and Li_3VO_4. Both ordered layered and DRX-$LiVO_2$ as well as ordered Li_3VO_4 have been explored as potential LIB anodes.[36−38] All three electrode materials have a cation:anion ratio of 1:1 and differ purely in their Li:V ratio and therefore active redox couple. Li_3VO_4 has a formal vanadium oxidation state of 5+, and all cations are ordered in tetrahedral sites. It can therefore be represented using the anion-normalized composition of $[Li_{0.75}V_{0.25}]^{tet}O$. In contrast, $LiVO_2$ has full octahedral occupancy like $Li_3V_2O_5$ and a formal V oxidation state of 3+. It can therefore be represented using the anion-normalized composition of $[Li_{0.5}V_{0.5}]^{oct}O$. It should be noted that Li_2O ($[Li_2]^{tet}O$) also has a cubic rocksalt structure with full occupancy in the tetrahedral sites and a cation:anion ratio of 2.

During charging, lithiation of $[Li_{0.6}V_{0.4}]^{oct}O$ occurs along the pathway indicated by the dashed blue line. The thermodynamically most favorable pathway is a conversion reaction given by the Li_2O−Li_3VO_4−$LiVO_2$ phase triangle ($[Li_2]^{tet}O$−$[Li_{0.75}V_{0.25}]^{tet}O$−$[Li_{0.5}V_{0.5}]^{oct}O$), in which case the DRX-$Li_3V_2O_5$ anode is converted to a mixture of $LiVO_2$, Li_2O, and V metal upon lithiation. However, kinetic considerations may favor lithium insertion instead of conversion. In contrast to Li ions, the redistribution of V ions is unlikely to occur due to the large migration barriers of V (1000−3500 meV) in the rocksalt lattice (Figure S1). This is in line with what has been observed experimentally.[5] The ultimate limit of insertion into rock salt $Li_{1-x}V_xO$ is given by the red dashed line representing $Li_{2-2x}V_xO$, i.e., a V^{2+} oxidation state. For a V cation content of 0.4, i.e., $Li_3V_2O_5$, this limit is given by $Li_{1.2}V_{0.4}O$ or $Li_6V_2O_5$. Experimentally, this limit is never reached and the highest lithiated state has a composition of $Li_1V_{0.4}O$ or $Li_5V_2O_5$.[5]

The insertion of Li^+ into the $Li_3V_2O_5$ anode at 0 K was studied by DFT calculations. Figure 2a shows the DFT-calculated pseudobinary $Li_3V_2O_5$−$Li_5V_2O_5$ phase diagram with the candidate structures colored in terms of their basis deformation. The larger the basis deformation, the greater the deviation of the DFT-relaxed structure from the ideal cubic rocksalt lattice. When x = 0, low-energy structures have low basis deformations and Li/V atoms are all in octahedral sites. When $x \geq 0.5$, the DFT ground states comprise phases that are highly distorted (basis deformation of >0.1) from the parent cubic rocksalt lattice; the cubic phases (basis deformation of ≤0.1) are metastable. A Li site occupancy analysis of DFT ground states structures (Figure 2b) indicates that redistribution of Li from octahedral sites to tetrahedral sites occurs when $x \sim 0.75$, where the occupancy of Li^{oct} sharply decreases to 0.1 and the occupancy of Li^{tet} increases to 0.65. These results are qualitatively in line with those of previous DFT studies.[5] However, this redistribution of Li is accompanied by a large volume change (∼20%) and lattice distortion, contradicting the experimental observation that the anode retains a stable cubic lattice with a small volume change of 5.9%.[5] In contrast, the Li site occupancy analysis of metastable cubic phases (Figure 2c) suggests that a redistribution of Li takes place only at the end of charging. The volume change of these metastable cubic phases ranges from 8% to 15%, which is much smaller than that of the Li redistributed configurations. The discrepancy between the DFT and experimental volume changes is likely due to the small cell size in calculations,

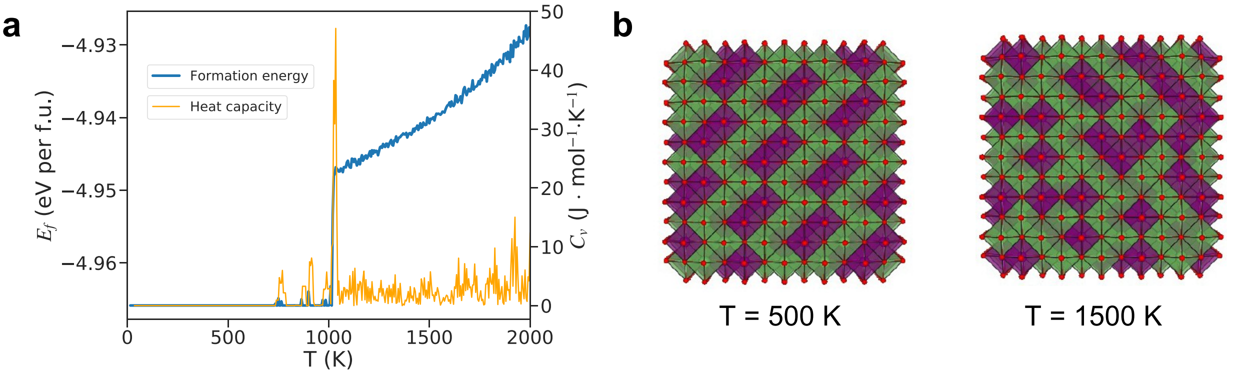

Figure 4. (a) Calculated formation energy (E_f) and heat capacity (C_v) as a function of temperature (T). (b) Structures from equilibrated Monte Carlo simulations at 500 and 1500 K. The MC simulations were initialized in the DFT-calculated most energetically stable $Li_3V_2O_5$ structure, in which all Li and V ions occupy the octahedral sites. The initial configuration was then heated from 10 to 2000 K in intervals of 10 K. At each temperature, the properties were then obtained by averaging the results from 1000 equilibrated MC runs. Configurational heat capacity C_v is given by the second derivative of formation energy E_f with respect to temperature T ($C_v = \partial^2 E_f/\partial^2 T$).

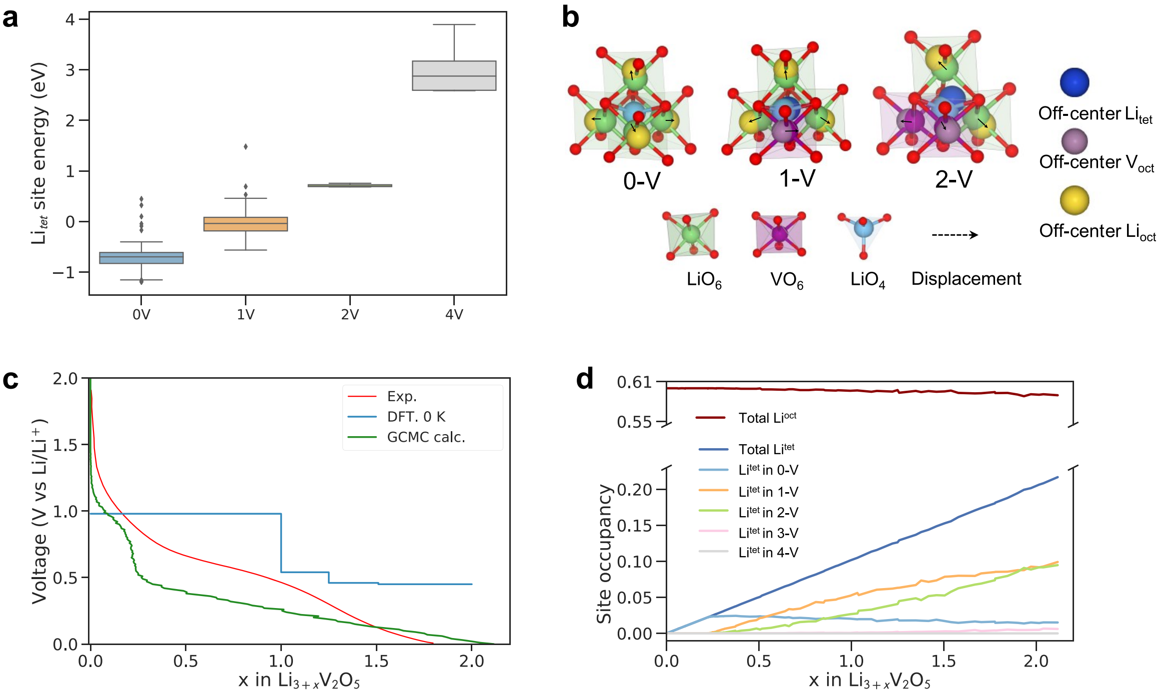

Figure 5. (a) Site energy of Li^{tet} in various local environments (i.e., diffusion sites). (b) 0-V, 1-V, and 2-V tetrahedral Li insertion sites and off-center displacements of the neighboring octahedral sites and the inserted tetrahedral Li sites. (c) Calculated voltage as a function of Li content x in $Li_{3+x}V_2O_5$. The experimental and DFT (0 K) results were taken from ref 5. (d) Evolution of Li site occupancies in tetrahedral and octahedral sites upon Li insertion from semi-GCMC simulations with the position of V^{oct} fixed.

differences in experimental versus DFT conditions, and well-known DFT errors in reproducing lattice parameters.[5]

Figure 2d shows the distribution of relative energies and the average Steinhardt order parameter ($\overline{D}_j$) of the initial $Li_3V_2O_5$ structures corresponding to the cubic and distorted lithiated $Li_{3+x}V_2O_5$ ($x \geq 1$) structures. One can see that the lithiated structures that maintain a cubic-like structure have greater $\overline{D}_j$ values, i.e., more Li/V disorder, and higher relative energies compared to the values of those that are highly distorted (see Figure S2b). These cubic-like structures also exhibit only moderate Li redistribution at the end of charging. In contrast, the low-DFT energy lithiated structures correspond to initial Li/V arrangements that are less disordered. In fact, the DFT ground state $Li_3V_2O_5$ exhibits an ordered layered-like Li/V arrangement akin to $LiVO_2$ with a $\overline{D}_j$ of 6×10^{-4}.

It should be noted that the initial Li/V disorder is controlled via synthesis levers such as temperature. Given that the as-synthesized DRX-$Li_3V_2O_5$ anode is highly cubic and exhibits Li/V disorder, we may surmise from the results presented above that the relevant lithiation pathway is one in which Li primarily inserts into the tetrahedral sites with minimal redistribution of Li^{oct} to Li^{tet} while maintaining a cubic-like framework with a low degree of distortion.

Validation of the Cluster Expansion Model. Figure 3a plots the 112 non-zero ECIs of the fitted CE model versus cluster size. It may be observed that the magnitude of the ECIs converges to near 0 at the cutoff radius. Figure 3b shows that the fitted CE model accurately captures the DFT-computed ground states (structures with formation energies on the convex hull).

Order−Disorder Transition of Cubic $Li_3V_2O_5$. To further understand the effect of cation disorder in the DRX-$Li_3V_2O_5$ anode, we performed Monte Carlo simulation using the fitted CE model. Figure 4 shows calculated formation energy E_f and specific heat capacity C_v as a function of temperature from MC simulations with the fitted CE model. The critical temperature (T_c) of the order−disorder phase transition is predicted to be ∼1000 K, which is somewhat lower than that experimentally measured for $LiVO_2$ (1775 K).[39] At temperatures below T_c, both E_f and C_v remain relatively constant with temperature, characteristic of a highly ordered crystal. At T_c, a discontinuous increase in E_f and a sharp peak in configurational C_v are observed, indicative of a phase transition taking place. The calculated average configurational specific heat capacity of the DRX phase ($T > 1000$ K) is 2.973 J mol^{-1} K^{-1}. Figure 4b shows two sampled configurations from the equilibrated MC simulations at 500 K (ordered phase) and 1500 K (fully disordered phase). At temperatures above T_c, Li/V disordering occurs mostly on the octahedral 4*b* sites and only a small fraction of Li (∼0.0125%) ions occupy the tetrahedral sites. These observations are consistent with the fact that the DRX is synthesized under the application of an external driving force, such as high temperatures, ball milling, or electrochemical lithiation.[5,6,40]

Lithium Intercalation Mechanism and Predicted Voltage Profile. The mechanism of intercalation of Li^+ into DRX structures is strongly affected by the distribution of the tetrahedral sites with different local environments and connectivity. The Li atoms in tetrahedral sites share faces with four neighboring octahedral sites. As shown in previous works,[1−3,5] the Li/transition metal occupancy of these neighboring octahedral sites has a strong influence on the local site occupancies and Li^+ migration barriers. The local environment of a tetrahedral site can be denoted by *n*-V (n = 0−4), where n represents the number of face-shared V octahedrons. Figure 5a shows the distribution of the calculated Li^{tet} site energies in 0-V, 1-V, 2-V, and 4-V clusters in the three SQSs with the lowest DFT energies. The Li_{tet} site energy in 3-V is not presented because Li_{tet} is unstable in this local environment and the electrostatic repulsive effect between the inserted Li_{tet} and the neighboring Li^{oct} ion caused local environment rearrangements during structure relaxations. In general, the Li_{tet} site energy and the distortion of neighboring LiO_6 octahedra increase with the number of neighboring V atoms. The Li insertion into 0-V sites is the most energetically favorable, and the four neighboring Li_{oct} sites are displaced off-center by 0.4−0.5 Å due to the electrostatic repulsion between Li^+ ions (Figure 5b). The 1-V Li_{tet} site energy is on average 660 meV higher than that of 0-V sites, and the inserted Li is displaced by ∼0.4 Å from the center of the tetrahedron in the direction away from the V ions. The off-center displacements of neighboring Li^{oct} are 0.3−0.6 Å, whereas those for the neighboring V^{oct} are only 0.16 Å. The 2-V Li^{tet} sites are relatively energetically unstable and are positioned ∼0.4 Å from the tetrahedral center due to strong repulsive interactions between V^{3+}/V^{4+} and Li^+. The neighboring Li atoms are pushed 0.5−0.6 Å from the center of the octahedron, causing large distortions in the local lattice structure.

The migration of V vacancies between neighboring octahedral sites was also investigated by introducing one V^{oct} vacancy into the configuration with the lowest V^{oct} vacancy energy. The average V^{oct} migration barrier is extremely high, ∼1000-3000 meV (Figure S1). This suggests that V ions in DRX-$Li_3V_2O_5$ are unlikely to migrate during charging and discharging under operating conditions.

Figure 5c shows the calculated voltage profile determined by GCMC simulations. The GCMC-predicted voltage profile exhibits a solid solution-like behavior and is in good agreement with the experimentally measured voltage profile.[5] Li starts to insert into DRX-$Li_3V_2O_5$ at ∼1.43 V, and the predicted voltage profile exhibits two voltage steps around 0.9 and 0.25 V versus Li/Li^+. As the voltage decreases to 0.01 V, the predicted average composition of the lithiated anode is $Li_{5.11}V_2O_5$, close to that observed in experiments ($Li_{4.86}V_2O_5$).[5] In contrast, due to the limited supercell sizes used, DFT calculations[5] predict multiple voltage steps at 0.98, 0.54, 0.46, and 0.45 V.

Figure 5d shows the evolution of Li site occupancies in DRX-$Li_{3+x}V_2O_5$ as a function of inserted Li content x. It should be noted that as an anode, insertion of Li into DRX-$Li_3V_2O_5$ corresponds to the charging process in a typical Li-ion battery. As Li ions are introduced into the tetrahedral sites, the Li occupancy in the octahedral sites first remains constant at around 0.6 until $x \approx 0.3$, following which there is a small, gradual decrease in Li^{oct} occupancy. The insertion of Li ions into the tetrahedral sites consists of two steps. Li^+ first intercalates into 0-V sites, which is consistent with the energies predicted by DFT calculations (Figure 5a) and previous results showing that the insertion into 0-V tetrahedral sites is the most energetically favorable.[5] This process coincides with the formation of the first plateau around 0.9 V on the voltage profile. When $x = 0.31$, 0-V sites are fully occupied and further lithiation insertion occurs in the energetically less favorable 1-V and 2-V sites. The occupancies of 1-V and 2-V sites increase to ∼0.1 until the end of charging. At the end of charging, only ∼0.1% of the 3-V tetrahedral sites are occupied and all 4-V sites are vacant.

We note that there are a few qualitative discrepancies between the experimental and GCMC voltage profiles, most notably, the absence of the voltage drop when $x \sim 0.31$. We have ascertained that this discrepancy can be attributed to the initial Li/V ordering in DRX-$Li_3V_2O_5$. The voltage profile in Figure 5c corresponds to the thermodynamically equilibrated structure, which exhibits a degree of ordering that differs from that of a truly random solid solution. This GCMC structure has a much lower fraction of 0-V sites (3.5%) compared to the random solid solution structure (13%). We have performed additional GCMC simulations on DRX-$Li_3V_2O_5$ with different Li/V orderings (Figure S6). With an increase in the level of initial disorder (and a larger fraction of 0-V sites), the voltage profile shifts upward and the sharp decrease at $x \sim 0.31$ disappears. It should be noted that we have no information about the Li/V ordering in the experimental DRX-$Li_3V_2O_5$ material, and the synthesis (electrochemical lithiation of V_2O_5) cannot be easily replicated via simulation. However, the effect of short-range ordering on the electrochemical properties of DRX electrodes has also been reported previously.[41] Another important potential source of the discrepancy is the fact that the GCMC voltage profile does not incorporate any kinetic effects, e.g., barriers to insertion and migration of Li, which may be present during electrochemical cycling.

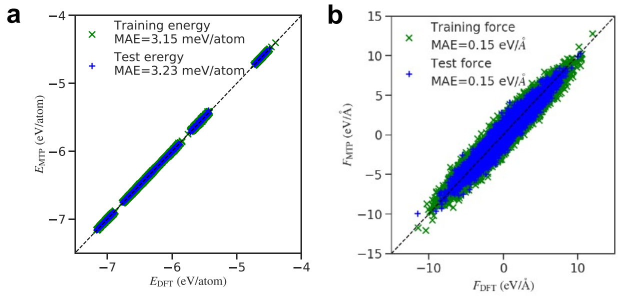

Figure 6. Plots of (a) MTP-predicted vs DFT energies and (b) MTP-predicted vs DFT forces with a lev_{max} of 20.

Validation of the Moment Tensor Potential. The mean absolute errors (MAEs) of training energies and forces (shown in Figure 6) of the fitted MTP are 3.15 meV atom^{-1} and 0.15 eV Å^{-1}, respectively, comparable to those of other MTPs in the literature.[42,43] As shown in Table 1, the MTP can accurately reproduce the lattice parameters and densities of training structures, with errors of ±3.12% and ±4.42% relative to DFT values, respectively.

Diffusion Properties. MD simulations were carried out to investigate the diffusion of Li$^+$ in the DRX-$Li_{3+x}V_2O_5$ anode as a function of Li concentration using the fitted MTP potential. The initial structures were obtained from the equilibrium semi-GCMC simulations in the preceding section. Figure 7 shows calculated diffusivity D_{Li^+} and activation energy E_a as a function of Li content x in DRX-$Li_{3+x}V_2O_5$ at room temperature (300 K). The Arrhenius plot from *NPT* MD simulations for each composition is shown in Figure S7. At the start of lithiation, a sharp increase in D_{Li^+} to ∼10^{-9} cm^2 s^{-1} with a corresponding decrease in E_a from ∼410 to ∼300 meV is observed up to x = 0.5. However, further lithiation results in a gradual decrease in D_{Li^+} from ∼10^{-9} to ∼10^{-11} cm^2 s^{-1} accompanied by an increase in E_a from ∼300 to 450 meV.

We further analyzed the Li$^+$ trajectories from 1 ns MD simulations at 600 K, and the results for selected configurations are presented in Figure 7b. When x < 1.5, Li$^+$ ions migrate via a cooperative tetrahedral−octahedral−tetrahedral (t−o−t) mechanism, in agreement with previous NEB calculations.[5] When x > 1.5, the increased amount of inserted Li$^+$ in tetrahedral sites and vacancies in octahedral sites may result in the migration of Li$^+$ between neighboring tetrahedral−tetrahedral (t−t) sites via the vacant octahedral sites along with the t−o−t migration.

To confirm the results presented above and further understand the Li$^+$ diffusion behaviors in different states of charge, DFT NEB calculations were also performed to calculate the Li$^+$ migration barriers. Similar to the previous NEB calculations,[5] a cooperative mechanism of Li$^+$ migration was considered, in which the tetrahedral Li$^+$ migrates to a neighboring octahedral site and the octahedral Li$^+$ migrates into another neighboring tetrahedral site (Figure 7c). Here, we consider cooperative migration that occurs between corner-sharing and opposing tetrahedral sites, given that migration between edge-sharing tetrahedral sites is extremely energetically unfavorable due to the proximity of the Li during migration (Figures S9c and S10c). Figure 7d shows the calculated Li$^+$ migration barriers between connected 0-V and 1-V sites. We note that migration from the 2-V site to the 0-V and 1-V sites is energetically downhill due to the large site energy differences (Figure S12). The cooperative migration of Li$^+$ via opposing t−o−t paths exhibits the lowest calculated average energy barriers, ranging from 230 to 340 meV in 0-V and 1-V sites. The average energy barriers of Li$^+$ transport through corner-sharing t−o−t pathways exhibit higher energy barriers of 334 to 628 meV. In general, the migration barriers of Li$^+$ increase as more V atoms gather around the local environment of tetrahedral Li$^+$ sites. These results are in line with those of the MD simulations. At the beginning of charging, few Li$^+$ ions are inserted into the anode and Li$^+$ diffusion is primarily mediated by vacancy migrations, which has high energy barriers ranging from 300 to 600 meV across the 0-V and 1-V sites (Figure S15). As the lithiation proceeds, the inserted Li$^+$ ions migrate predominantly via a cooperative mechanism. Thus, the activation energy of Li$^+$ transport first decreases as the inserted Li$^+$ ions first occupy 0-V sites and then increases gradually as more Li$^+$ ions diffuse via slower tunnels. At the end of charging, the formation of vacancies at the octahedral sites allows for direct hopping of Li$^+$ from one tetrahedral site to its next edge-sharing tetrahedral site (t−t), as illustrated in Figure S13, with a low energy barrier of 241 meV. These results are in line with the activation energies obtained by MD simulations and previous theoretical studies[5] showing that the facile migration of Li$^+$ across opposing t−o−t pathways results in the high rate capability of the DRX-$Li_{3+x}V_2O_5$ anode. In previous studies,[5] Li$^+$ hopping via 0-V sites is the only mechanism that was considered while our results show that Li$^+$ migration in 0-V, 1-V, and 2-V sites is facile. Similar results have also been observed in LTO anodes in which the transportation of Li$^+$ in a face-sharing octahedral−tetrahedral motif contributes to fast kinetics.[44]

■ CONCLUSIONS

A major conclusion from this work is that the lithium insertion mechanism in $Li_3V_2O_5$ strongly depends on the initial Li/V

Table 1. Lattice Parameters and Densities of the Structures in the Training Set (zero strain) Relaxed with the Trained MTP at 0 K, in Comparison with DFT-Calculated Lattice Parameters and Densities at 0 K[a]

composition	*a* (Å)	*b* (Å)	*c* (Å)	density (g/cm^3)
$LiVO_2$	3.02 (1.75%)	5.16 (−1.24%)	5.25 (1.19%)	3.88 (1.69%)
LiV_2O_5	6.75 (0.98%)	7.68 (0.41%)	7.58 (−1.65%)	3.18 (−0.28%)
Li_3VO_4	5.06 (0.48%)	5.54 (0.51%)	6.37 (−0.41%)	2.52 (−0.57%)
Li_2O	3.30 (0.056%)	3.29 (0.056%)	3.29 (0.056%)	1.96 (−0.17%)
DRX-$Li_3V_2O_5$	8.46 (0.66%)	8.45 (1.26%)	8.42 (0.84%)	3.60 (−2.71%)
DRX-$Li_{3.9}V_2O_5$	8.62 (1.26%)	8.62 (1.25%)	8.62 (1.24%)	3.18 (−3.66%)
DRX-$Li_5V_2O_5$	9.48 (3.12%)	7.72 (−1.03%)	9.43 (2.519%)	3.36 (−4.42%)

[a] Values in parentheses are the percentage differences between the MTP- and DFT-computed values.

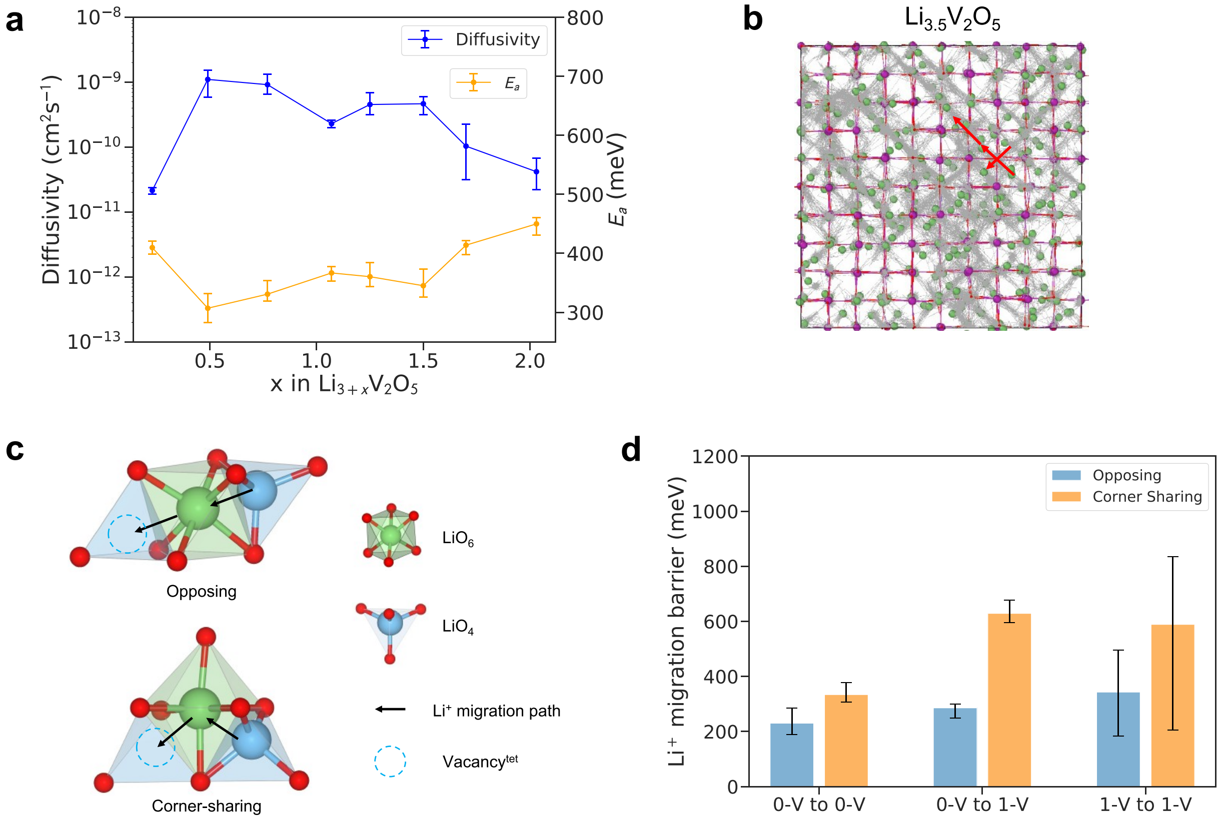

Figure 7. (a) Calculated diffusivity and activation energy of Li^+ in DRX-$Li_{3+x}V_2O_5$ as a function of Li content at 300 K. The diffusivities and activation energies were calculated from configurations generated by three independent GCMC simulations. The error bars are for the standard deviations of diffusivities and activation energies. (b) Li trajectories (colored gray) from MD simulations of $Li_{3.5}V_2O_5$ at 600 K, projected in the crystallographic $a-b$ planes. Illustrations of t−o−t migration mechanisms of Li^+ are shown with red arrows. The green, purple, and red spheres represent Li, V, and O atoms, respectively. (c) Illustration of the Li^+ migration path in DRX-$Li_3V_2O_5$. The opposing and corner-sharing pathways indicate cooperative migration mechanisms of Li^+ via the octahedral site and its next tetrahedral site. (d) Calculated NEB barriers for possible Li migration hops. The barriers are categorized in terms of their mechanisms and local environments.

disorder. For highly ordered Li/V arrangements with lower energies, Li insertion occurs via a redistribution mechanism with the formation of highly distorted structures and accompanied by large volume changes. This is consistent with previous DFT results but inconsistent with experimental observations for the DRX-$Li_3V_2O_5$ electrode.[5] In contrast, Li/V disorder leads to Li inserting primarily into the tetrahedral sites, while retaining a cubic-like structure with small volume changes. The MC-predicted voltage profile based on this latter mechanism is also in much better agreement with the experimental voltage profile.

The Li^+ insertion mechanism and transport depend on the local environment around each tetrahedral site and the distribution of sites. Our results show that Li^+ ions in 0-V sites are the most energetically favorable and have the lowest migration barrier and ≥2-V sites are highly energetically unfavorable. Assuming a fully cation-disordered DRX-$Li_3V_2O_5$ ($[Li_{0.6}V_{0.4}]^{oct}O$), the probability of an n-V site $P(n)$ is given by the binomial distribution

$$P(n) = \frac{4!}{n!(4-n)!} \times 0.4^n \times 0.6^{4-n} \tag{10}$$

The fractions of 0-V, 1-V, and ≥2-V are therefore 0.13, 0.35, and 0.52, respectively. The highest experimentally realized lithiation state is $Li_5V_2O_5$ (~$Li_1V_{0.4}O$), which approximately corresponds to the full occupancy of the most energetically favored 0-V sites and ~0.77 occupancy of the 1-V tetrahedral sites. Hence, we can surmise that the inability of DRX-$Li_{3+x}V_2O_5$ to reach the theoretical V^{2+} limit of $Li_6V_2O_5$ is due to the lack of low-energy sites for further Li insertion.

Our analysis suggests that one potential avenue for tuning the electrochemical properties of the DRX anode is by varying the Li:V ratio in $[Li_{1-x}V_x]^{oct}O$. Increasing the Li:V ratio would increase the fraction of 0-V and 1-V tetrahedral sites, but at the price of increasing the V oxidation state and, hence, the anode voltage. Conversely, decreasing the Li:V ratio would decrease the lithiation capacity but also decrease the anode voltage. The optimal ratio would depend on the specific application, for example, whether a high rate or a high-energy density anode is prioritized.

■ ASSOCIATED CONTENT

Supporting Information

The Supporting Information is available free of charge at https://pubs.acs.org/doi/10.1021/acs.chemmater.2c02839.

NEB barriers for V^{4+}/V^{3+} migration and illustration of the minimum energy path of V atoms (Figure S1), relative energies of $LiVO_2$ and $Li_3V_2O_5$ structures as a function of the order parameter and crystal structure of the calculated ground state $R\bar{3}m$ $LiVO_2$ and $Li_3V_2O_5$ (Figure S2), structures of the lowest-energy metastable cubic phase and the ground state of $Li_{3+x}V_2O_5$ (Figure S3), CV score and RMSE of the fitted CE model as a function of the regularization parameter (Figure S4), MC simulations of the order−disorder phase transition of $Li_3V_2O_5$ in the 10 × 10 × 10 supercell (Figure S5), distribution of tetrahedral sites in different local environments obtained from averaging 10 equilibrated 5 × 5 × 5 cells from independent MC simulations at 1500 K (Figure S6), calculated voltage as a function of Li content x in $Li_{3+x}V_2O_5$ from GCMC simulations with different initial Li/V orderings with different fractions of 0-V sites (Figure S7), illustration of the Li/V orderings at 0 and 1500 K MC-equilibrated and random solid solution structures of $Li_3V_2O_5$ (Figure S8), Arrhenius plot from *NPT* MD simulations of $Li_{3+x}V_2O_5$ (Figure S9), calculated Li^+ trajectories obtained from MD simulations (Figure S10), DFT-calculated Li^+ migration barriers via 0-V sites, 0-V and 1-V sites, *i-V* sites, and connected 1-V and 2-V sites (opposing) (Figure S11), illustration of Li^+ migration via the edge-sharing t−o−t path in DRX-$Li_3V_2O_5$ (Figure S12), illustration of Li^+ migration via the t−t path in DRX-$Li_3V_2O_5$ (Figure S13), and calculated NEB barriers for possible vacancy migration hops (Figure S14) (PDF)

AUTHOR INFORMATION

Corresponding Author

Shyue Ping Ong − *Department of Nanoengineering, University of California San Diego, La Jolla, California 92093, United States;* orcid.org/0000-0001-5726-2587; Email: ongsp@eng.ucsd.edu

Authors

Xingyu Guo − *Materials Science and Engineering Program, University of California San Diego, La Jolla, California 92093-0448, United States;* orcid.org/0000-0002-3456-5347

Chi Chen − *Department of Nanoengineering, University of California San Diego, La Jolla, California 92093, United States;* orcid.org/0000-0001-8008-7043

Complete contact information is available at: https://pubs.acs.org/10.1021/acs.chemmater.2c02839

Notes

The authors declare no competing financial interest.

ACKNOWLEDGMENTS

This work is supported by the Materials Project, funded by the U.S. Department of Energy, Office of Science, Office of Basic Energy Sciences, Materials Sciences and Engineering Division, under Contract DEAC02-05-CH11231 (Materials Project Program KC23MP). The authors acknowledge the computing resources provided by Triton Shared Computing Cluster (TSCC) at the University of California San Diego, the National Energy Research Scientific Computing Center (NERSC), and the Extreme Science and Engineering Discovery Environment (XSEDE) supported by the National Science Foundation, under Grant ACI-1053575. The authors also acknowledge extremely helpful discussions with Dr. Sanjeev Kolli and Prof. Anton van der Ven of the University of California Santa Barbara on the use of the CASM code.

REFERENCES

(1) Clément, R.; Lun, Z.; Ceder, G. Cation-disordered rocksalt transition metal oxides and oxyfluorides for high energy lithium-ion cathodes. *Energy Environ. Sci.* **2020**, *13*, 345−373.

(2) Lee, J.; Urban, A.; Li, X.; Su, D.; Hautier, G.; Ceder, G. Unlocking the potential of cation-disordered oxides for rechargeable lithium batteries. *science* **2014**, *343*, 519−522.

(3) Urban, A.; Matts, I.; Abdellahi, A.; Ceder, G. Computational design and preparation of cation-disordered oxides for high-energy-density Li-ion batteries. *Adv. Energy Mater.* **2016**, *6*, 1600488.

(4) Kitchaev, D. A.; Lun, Z.; Richards, W. D.; Ji, H.; Clément, R. J.; Balasubramanian, M.; Kwon, D.-H.; Dai, K.; Papp, J. K.; Lei, T.; et al. Design principles for high transition metal capacity in disordered rocksalt Li-ion cathodes. *Energy Environ. Sci.* **2018**, *11*, 2159−2171.

(5) Liu, H.; Zhu, Z.; Yan, Q.; Yu, S.; He, X.; Chen, Y.; Zhang, R.; Ma, L.; Liu, T.; Li, M.; et al. A disordered rock salt anode for fast-charging lithium-ion batteries. *Nature* **2020**, *585*, 63−67.

(6) Barnes, P.; Zuo, Y.; Dixon, K.; Hou, D.; Lee, S.; Ma, Z.; Connell, J. G.; Zhou, H.; Deng, C.; Smith, K.; et al. Electrochemically induced amorphous-to-rock-salt phase transformation in niobium oxide electrode for Li-ion batteries. *Nat. Mater.* **2022**, *21*, 795.

(7) Xiong, H.; Slater, M. D.; Balasubramanian, M.; Johnson, C. S.; Rajh, T. Amorphous TiO2 nanotube anode for rechargeable sodium ion batteries. *journal of physical chemistry letters* **2011**, *2*, 2560−2565.

(8) Zhang, W.; Liang, J.; Zhu, Y.; Qian, Y.; et al. Facile synthesis and electrochemistry of a new cubic rocksalt Li x V y O 2 (x= 0.78, y= 0.75) electrode material. *Journal of Materials Chemistry A* **2017**, *5*, 5148−5155.

(9) Zunger, A.; Wei, S.-H.; Ferreira, L.; Bernard, J. E. Special quasirandom structures. *Physical review letters* **1990**, *65*, 353.

(10) Kresse, G.; Furthmüller, J. Efficient iterative schemes for ab initio total-energy calculations using a plane-wave basis set. *Phys. Rev. B* **1996**, *54*, 11169.

(11) Blöchl, P. E. Projector augmented-wave method. *Phys. Rev. B* **1994**, *50*, 17953.

(12) Perdew, J. P.; Burke, K.; Ernzerhof, M. Generalized gradient approximation made simple. *Physical review letters* **1996**, *77*, 3865.

(13) Dudarev, S.; Botton, G.; Savrasov, S.; Humphreys, C.; Sutton, A. Electron-energy-loss spectra and the structural stability of nickel oxide: An LSDA+ U study. *Phys. Rev. B* **1998**, *57*, 1505.

(14) Jain, A.; Hautier, G.; Ong, S. P.; Moore, C. J.; Fischer, C. C.; Persson, K. A.; Ceder, G. Formation enthalpies by mixing GGA and GGA+ U calculations. *Phys. Rev. B* **2011**, *84*, 045115.

(15) Jain, A.; Ong, S. P.; Hautier, G.; Chen, W.; Richards, W. D.; Dacek, S.; Cholia, S.; Gunter, D.; Skinner, D.; Ceder, G.; et al. Commentary: The Materials Project: A materials genome approach to accelerating materials innovation. *Apl Materials* **2013**, *1*, 011002.

(16) Kawasaki, T.; Onuki, A. Construction of a disorder variable from Steinhardt order parameters in binary mixtures at high densities in three dimensions. *J. Chem. Phys.* **2011**, *135*, 174109.

(17) Menon, S.; Leines, G. D.; Rogal, J. pyscal: A python module for structural analysis of atomic environments. *Journal of Open Source Software* **2019**, *4*, 1824.

(18) Van der Ven, A.; Thomas, J.; Xu, Q.; Bhattacharya, J. Linking the electronic structure of solids to their thermodynamic and kinetic properties. *Mathematics and computers in simulation* **2010**, *80*, 1393−1410.

(19) Sanchez, J. M.; Ducastelle, F.; Gratias, D. Generalized cluster description of multicomponent systems. *Physica A: Statistical Mechanics and its Applications* **1984**, *128*, 334−350.

(20) De Fontaine, D. Cluster approach to order-disorder transformations in alloys. *Solid State Phys.* **1994**, *47*, 33−176.

(21) Thomas, J. C.; Van der Ven, A. Finite-temperature properties of strongly anharmonic and mechanically unstable crystal phases from first principles. *Phys. Rev. B* **2013**, *88*, 214111.

(22) *CASM*, ver. 1.1.1; 2021 (https://github.com/prisms-center/CASMcode).

(23) Li, W.; Reimers, J.; Dahn, J. Lattice-gas-model approach to understanding the structures of lithium transition-metal oxides LiM O 2. *Phys. Rev. B* **1994**, *49*, 826.

(24) Novikov, I. S.; Gubaev, K.; Podryabinkin, E. V.; Shapeev, A. V. The MLIP package: moment tensor potentials with MPI and active learning. *Machine Learning: Science and Technology* **2021**, *2*, 025002.

(25) Qi, J.; Banerjee, S.; Zuo, Y.; Chen, C.; Zhu, Z.; Holekevi Chandrappa, M. L.; Li, X.; Ong, S. P. Bridging the gap between simulated and experimental ionic conductivities in lithium superionic conductors. *Mater. Today Phys.* **2021**, *21*, 100463.

(26) Nosé, S. A unified formulation of the constant temperature molecular dynamics methods. *J. Chem. Phys.* **1984**, *81*, 511−519.

(27) Hoover, W. G. Canonical dynamics: Equilibrium phase-space distributions. *Phys. Rev. A* **1985**, *31*, 1695.

(28) Shapeev, A. V. Moment tensor potentials: A class of systematically improvable interatomic potentials. *Multiscale Modeling & Simulation* **2016**, *14*, 1153−1173.

(29) Gubaev, K.; Podryabinkin, E. V.; Hart, G. L.; Shapeev, A. V. Accelerating high-throughput searches for new alloys with active learning of interatomic potentials. *Comput. Mater. Sci.* **2019**, *156*, 148−156.

(30) Thompson, A. P.; Aktulga, H. M.; Berger, R.; Bolintineanu, D. S.; Brown, W. M.; Crozier, P. S.; in't Veld, P. J.; Kohlmeyer, A.; Moore, S. G.; Nguyen, T. D.; et al. LAMMPS-a flexible simulation tool for particle-based materials modeling at the atomic, meso, and continuum scales. *Comput. Phys. Commun.* **2022**, *271*, 108171.

(31) Chen, C.; Yunxing Zuo, Q. J.; Weike, Y.; Ong, S. P. *Maml - materials machine learning package*; 2020 (https://github.com/materialsvirtuallab/maml).

(32) Henkelman, G.; Uberuaga, B. P.; Jónsson, H. A climbing image nudged elastic band method for finding saddle points and minimum energy paths. *J. Chem. Phys.* **2000**, *113*, 9901−9904.

(33) Henkelman, G.; Jónsson, H. Improved tangent estimate in the nudged elastic band method for finding minimum energy paths and saddle points. *J. Chem. Phys.* **2000**, *113*, 9978−9985.

(34) Van der Ven, A.; Ceder, G.; Asta, M.; Tepesch, P. First-principles theory of ionic diffusion with nondilute carriers. *Phys. Rev. B* **2001**, *64*, 184307.

(35) Ong, S. P.; Chevrier, V. L.; Hautier, G.; Jain, A.; Moore, C.; Kim, S.; Ma, X.; Ceder, G. Voltage, stability and diffusion barrier differences between sodium-ion and lithium-ion intercalation materials. *Energy Environ. Sci.* **2011**, *4*, 3680−3688.

(36) Armstrong, A. R.; Lyness, C.; Panchmatia, P. M.; Islam, M. S.; Bruce, P. G. The lithium intercalation process in the low-voltage lithium battery anode Li1+ xV1- xO2. *Nature materials* **2011**, *10*, 223−229.

(37) Li, H.; Liu, X.; Zhai, T.; Li, D.; Zhou, H. Li3VO4: a promising insertion anode material for lithium-ion batteries. *Adv. Energy Mater.* **2013**, *3*, 428−432.

(38) Baur, C.; Chable, J.; Klein, F.; Chakravadhanula, V. S. K.; Fichtner, M. Reversible delithiation of disordered rock salt LiVO2. *ChemElectroChem.* **2018**, *5*, 1484−1490.

(39) Hewston, T.; Chamberland, B. A survey of first-row ternary oxides LiMO2 (M= Sc-Cu). *J. Phys. Chem. Solids* **1987**, *48*, 97−108.

(40) Delmas, C.; Cognac-Auradou, H. Formation of the ω-type phase by lithium intercalation in (Mo, V) oxides deriving from V2O5. *J. Power Sources* **1995**, *54*, 406−410.

(41) Ji, H.; Urban, A.; Kitchaev, D. A.; Kwon, D.-H.; Artrith, N.; Ophus, C.; Huang, W.; Cai, Z.; Shi, T.; Kim, J. C.; et al. Hidden structural and chemical order controls lithium transport in cation-disordered oxides for rechargeable batteries. *Nat. Commun.* **2019**, *10*, 592.

(42) Zuo, Y.; Chen, C.; Li, X.; Deng, Z.; Chen, Y.; Behler, J.; Csányi, G.; Shapeev, A. V.; Thompson, A. P.; Wood, M. A.; et al. Performance and cost assessment of machine learning interatomic potentials. *J. Phys. Chem. A* **2020**, *124*, 731−745.

(43) Wang, C.; Aoyagi, K.; Wisesa, P.; Mueller, T. Lithium ion conduction in cathode coating materials from on-the-fly machine learning. *Chem. Mater.* **2020**, *32*, 3741−3752.

(44) Zhang, W.; Seo, D.-H.; Chen, T.; Wu, L.; Topsakal, M.; Zhu, Y.; Lu, D.; Ceder, G.; Wang, F. Kinetic pathways of ionic transport in fast-charging lithium titanate. *Science* **2020**, *367*, 1030−1034.

https://doi.org/10.1021/acs.chemmater.2c02839
Chem. Mater. XXXX, XXX, XXX−XXX